Journal of
Low Power Electronics and Applications

MDPI

Article

Multichannel Sensor Array Design for Minimizing Detector Complexity and Power Consumption in Ionoacoustic Proton Beam Tomography

Elia Arturo Vallicelli [1,*], Alessandro Michele Ferrara [1,2], Maurizio Marrale [2,3], Mattia Tambaro [1] and Marcello De Matteis [1]

[1] Department of Physics, University and INFN Section of Milano–Bicocca, 20126 Milano, Italy
[2] Department of Physics and Chemistry "Emilio Segrè" and Advanced Technologies Network Center, University of Palermo, 90126 Palermo, Italy
[3] Istituto Nazionale di Fisica Nucleare (INFN), Catania Division, 95123 Catania, Italy
* Correspondence: eliaarturo.vallicelli@unimib.it

Abstract: Ionoacoustic tomography exploits the acoustic signal generated by the fast energy deposition along the path of pulsed particle beams to reconstruct with sub-mm precision the dose deposition, with promising envisioned applications in hadron therapy treatment monitoring. State-of-the-art ionoacoustic detectors mainly rely on single-channel sensors and time-of-flight measurements to provide 1D localization of the maximum dose deposition at the so-called Bragg peak. This work investigates the design challenges of multichannel sensors for ionoacoustic tomography in terms of their ability to accurately reconstruct the dose deposition of a 200 MeV clinical proton beam, highlighting the impact of the number of channels in the array and their directivity. A complete acoustic model of the sensors and environment has been developed and used to find an optimum tradeoff between accuracy, evaluated numerically through the gamma index, and hardware complexity due to higher channel numbers, thus minimizing the system-level power consumption of the detector.

Keywords: circuits and systems for biomedical applications; radiation therapy; ultrasound sensors

Citation: Vallicelli, E.A.; Ferrara, A.M.; Marrale, M.; Tambaro, M.; De Matteis, M. Multichannel Sensor Array Design for Minimizing Detector Complexity and Power Consumption in Ionoacoustic Proton Beam Tomography. *J. Low Power Electron. Appl.* **2024**, *14*, 51. https://doi.org/10.3390/jlpea14040051

Academic Editor: Pak Kwong Chan

Received: 27 August 2024
Revised: 4 October 2024
Accepted: 6 October 2024
Published: 30 October 2024

1. Introduction

Ionoacoustic imaging exploits the acoustic wave generated by the rapid energy deposition along the range of a particle beam to precisely map the dose distribution in space. The rapid energy deposition generates a localized pressure increase proportional to the dose deposited via the ionoacoustic effect. This pressure wave propagates in the energy absorber (usually a water phantom) and can be acquired by an array of ultrasound sensors and processed by dedicated acoustic imaging algorithms [1–19]. One of the most interesting applications of ionoacoustic imaging is in beam monitoring in oncological hadron therapy, where it promises imaging performances competitive or better than traditional nuclear imaging techniques (e.g., PET) [19]. However, the literature has mainly focused on simple single-sensor time-of-flight measurements, and a detailed analysis of the sizing of the acoustic sensor array and its impact on the image reconstruction accuracy is lacking. For this reason, this paper addresses the sizing of the ultrasound array, highlighting the effect of the number of channels and their physical size.

This work aims to analyze the impact of the design of the multichannel acoustic sensor (in terms of number of channels and channel directivity) on its ability to accurately reconstruct the dose deposition. The cross-domain modeling of the system allowed us to find the minimum number of channels to reach an acceptable accuracy threshold, represented by the gamma index, a parameter commonly used in dosimetry. Minimizing the number of sensor channels is of fundamental importance to reduce power consumption (both electrical and computational) and the complexity of the final detector, since the number of channels impacts the following:

- The number of analog front-ends needed to interface with the sensor and amplify the signal, with typical specifications of 60 dB of gain, MHz of bandwidth, and a noise power spectral density of a few nV/sqrt(Hz). The acquisition must be parallel (one front-end per channel) since the information of each sensor must be acquired for each pulse of the particle beam.
- The number of analog-to-digital converters, with typical resolution specifications of 8–10 bits and oversampling 20–40 times the signal bandwidth (25 MS/s).
- The number of DSP denoising and equalization stages used to reject out-of-band noise and preserve the shape of the signal in the time domain, which is necessary to accurately reconstruct the dose deposition.
- The number of signals that the acoustic imaging algorithm must process to reconstruct the dose deposition.

This work is organized as follows. Section 2 will present the typical ionoacoustic setup, the characteristics of the acoustic signal, and the tradeoff between directivity and the number of sensor channels. Section 3 will describe the effect of sensor sizing on imaging performance. Finally, Section 4 will draw conclusions.

2. Materials and Methods

2.1. Ionoacoustic Experimental Setup Model

A typical ionoacoustic setup is shown in Figure 1. A 200 MeV proton beam penetrates a water absorber (water phantom) for about 26 cm, where the maximum dose deposition, called Bragg peak, occurs [1]. This study considers a circular array of sensors with a radius of 18 cm positioned around the proton beam, as shown in Figure 1. Each sensor acquires the signal from the particle beam under a different angle.

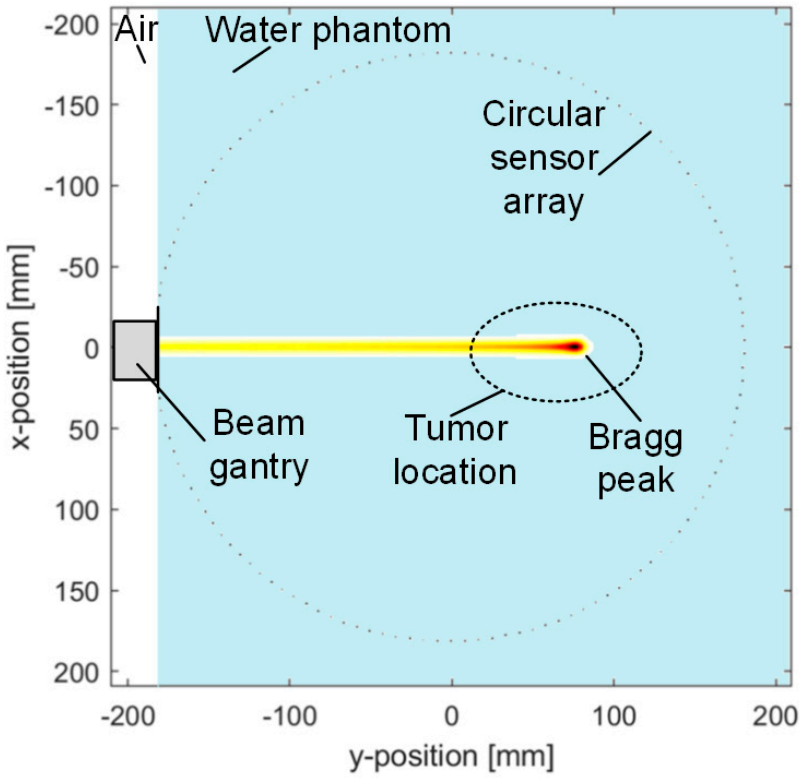

Figure 1. Experimental setup scheme.

The spectrum of the acquired acoustic signal depends on the source cross −section in the direction between the sensor and the source itself, where thinner sources will generate higher frequency signals. In particular, as a first approximation, the source cross-section is equal to half the wavelength of the generated acoustic signal. The typical acoustic signal

generated in this scenario has approximately the shape of a single sinusoid period with a main frequency of around 40 kHz. The amplitude depends on the dose deposited in the single pulse and is about 1 Pa at the source and a few tens of mPa at the sensor surface. Figure 2 shows the simulated time signal, acquired by a sensor placed in line with the beam. The information acquired by each sensor is used by acoustic imaging algorithms to reconstruct the image of the source. In this paper, this scenario has been simulated using k-Wave for both the simulation of the physical phenomenon and the time-reversal algorithm used for image reconstruction.

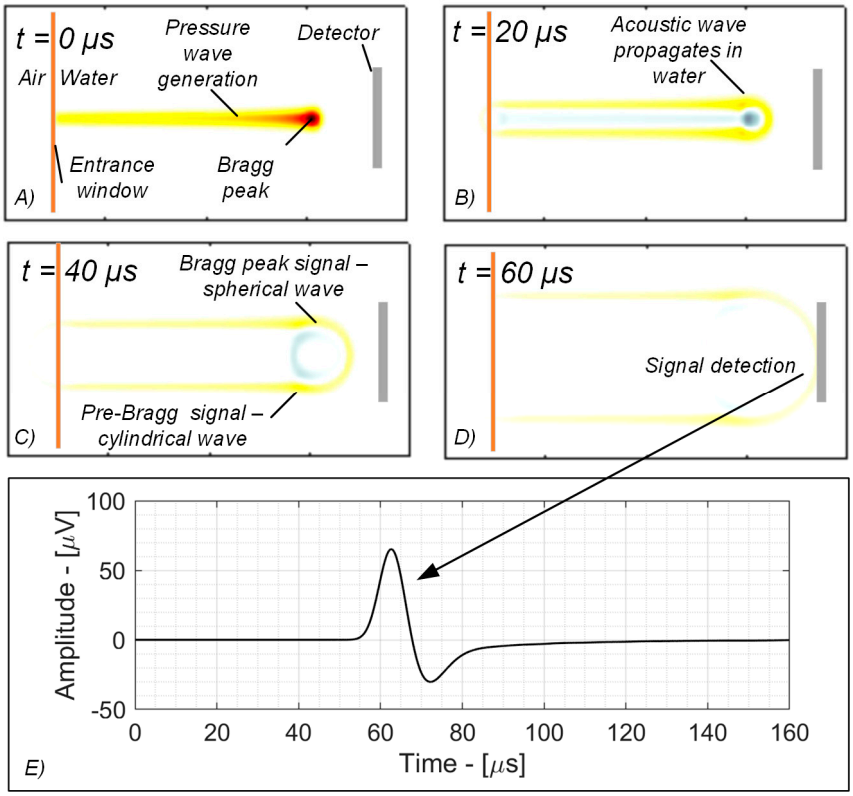

Figure 2. Different frames of acoustic wave simulation from (**A**) beam pulse to (**B**,**C**) signal propagation and (**D**) signal detection, and (**E**) typical ionoacoustic signal at sensor output from 200 MeV proton beam.

2.2. Acoustic Sensor Modeling

Typical sensors used in ionoacoustic experiments are piezoelectric. Piezoelectrics are transducers that convert a mechanical stimulus (such as a pressure wave) into an electrical signal. They are characterized by an approximately flat bandwidth and a resonant frequency where a peak is present, the height of which depends on the characteristics of the material and the acoustic coupling between the material and the surrounding environment (water or biological tissue). Most of the works in the literature use piezoceramic materials (Lead-Zirconate-Titanate, PZT) [6–19]. However, these are characterized by a strong resonance and a rather narrow bandwidth. The impulsive nature of ionoacoustic signals implies that their bandwidth is relatively wide, and the use of narrow-band sensors leads to a loss of information and distortion in the acquired signal, which ultimately appears as a distortion in the acquired acoustic image if not compensated by digital equalization stages. For this reason, this work considers piezo-polymer sensors (Polyvinyl difluoride, PVDF) characterized by better acoustic coupling with the surrounding environment and an intrinsically wider and flatter bandwidth. Furthermore, their plastic nature makes them much easier to machine and form into arrays of the desired size [20,21]. Compared to PZTs, their piezoelectric voltage constant is about an order of magnitude larger, while

the relative dielectric constant is an order of magnitude lower. This implies that both the transduced signal and its noise are an order of magnitude larger than those of PZTs, while the signal-to-noise ratio is comparable or slightly lower. Table 1 shows a comparison between the main parameters of PZTs and PVDFs, whereas Table 2 summarizes the main PVDF parameters.

Table 1. Comparison between PVDF and PZT piezoelectric materials' performance.

Parameter for unit area	PVDF w.r.t. PZT
Relative noise power	+20 dB
Relative Sensitivity	+17 dB
Relative SNR (Sensor only)	−3 dB
Relative SNR (Sensor + AFE)	+2 dB

Table 2. Typical PVDF parameters.

Parameter	Symbol	Value
Frequency coefficient	N_f	1125 Hz·m
Resonant frequency	f_r	800 kHz
Piezoelectric voltage coefficient	g_{33}	400 mV/(Pa·m)
Piezoelectric relative dielectric constant	ε_r	8
Channel width	W	3 mm
Channel length	L	30 mm
PVDF thickness	TH	1.2 mm
Water acoustic impedance	Z_w	1.5 MRayl
PVDF acoustic impedance	Z_{PVDF}	3.3 MRayl
Sensitivity	S	480 μV/Pa

The behavior of piezoelectrics depends not only on their material but also on their physical size. The thickness determines the resonant frequency and therefore the bandwidth of the sensor, according to Equation (1), where N is a constant that depends on the material and Th is the thickness of the sensor.

$$f_R = \frac{N}{Th} \tag{1}$$

The sensitivity of the sensor depends in turn on the thickness Th and piezoelectric voltage constant g_{33}, as in Equation (2).

$$S = g_{33} \cdot TH \tag{2}$$

The total area of the sensor determines its capacitance according to the formula for parallel plane-face capacitors, as shown in Equation (3).

$$C = \varepsilon_0 \varepsilon_r \frac{A}{Th} \tag{3}$$

In turn, the capacitance of the sensor determines in the first approximation its noise according to Equation (4).

$$ORN = \sqrt{\frac{kT}{C}} = \sqrt{\frac{k\ T\ Th}{\varepsilon_0 \varepsilon_r\ A}} \tag{4}$$

Its input-referred noise can be thus obtained with Equation (5).

$$IRN_{AS} = \frac{ORN_{AS}}{S} = \frac{1}{g_{33}}\sqrt{\frac{kT}{\varepsilon_0\varepsilon_r \cdot A \cdot Th}} \tag{5}$$

Therefore, thicker sensors will have a lower bandwidth, a higher sensitivity, and a higher noise.

If a sensor array is considered, each channel will be a piezoelectric with a noise dependent on its area and uncorrelated with respect to that of other channels. Instead, the signal acquired by each channel will be deterministic and these signals will be used by acoustic imaging algorithms to generate the image of the source. The noise will instead be decreased according to Equation (6).

$$SNR_{Nch} = SNR_{1Ch} + 10\log_{10} N_{ch} \tag{6}$$

Therefore, a sensor with N_{ch} channels will have a noise equal to that of a single-channel sensor with an area N_{ch} times larger.

Piezoelectric arrays therefore have a noise that depends on the total area of the array, while the performance of the single channel depends on its width. In fact, ideally, a sensor in an array must be able to acquire signals coming from any direction (omnidirectional). However, real sensors of finite dimensions are characterized by a certain directivity that depends on the ratio between their physical size and the wavelength of the signal.

In fact, if the wavelength is comparable or smaller than the sensor width, wavefronts reaching the sensor with a non-perpendicular arrival angle will touch different points of the sensor at different times. Therefore, each point of the sensor will transduce a signal that is not in phase with the adjacent points, causing destructive interference and a loss of sensitivity. The directivity of a sensor with regard to the angle of arrival θ, defined as the direction of arrival of the acoustic wavefront measured from the normal to the surface, follows Equation (7), while in Figure 3 the antenna patterns on the sensor plane for different channel sizes (from 75 mm to 4.5 mm) at 50 and 150 kHz can be observed.

$$\frac{S(\theta)}{S} = dir(\theta) = sinc\left(\frac{\pi f L sin(\theta)}{c_w}\right) \tag{7}$$

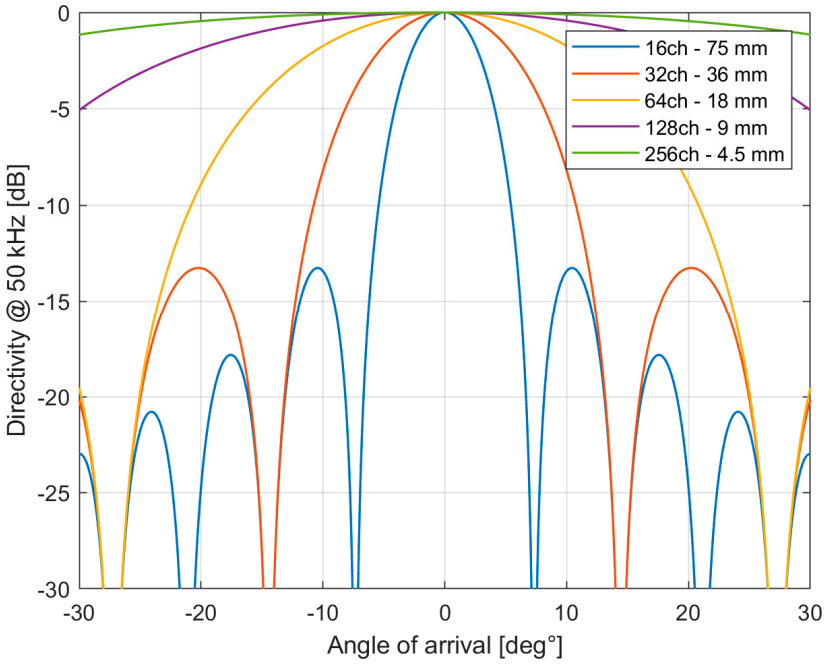

Figure 3. *Cont.*

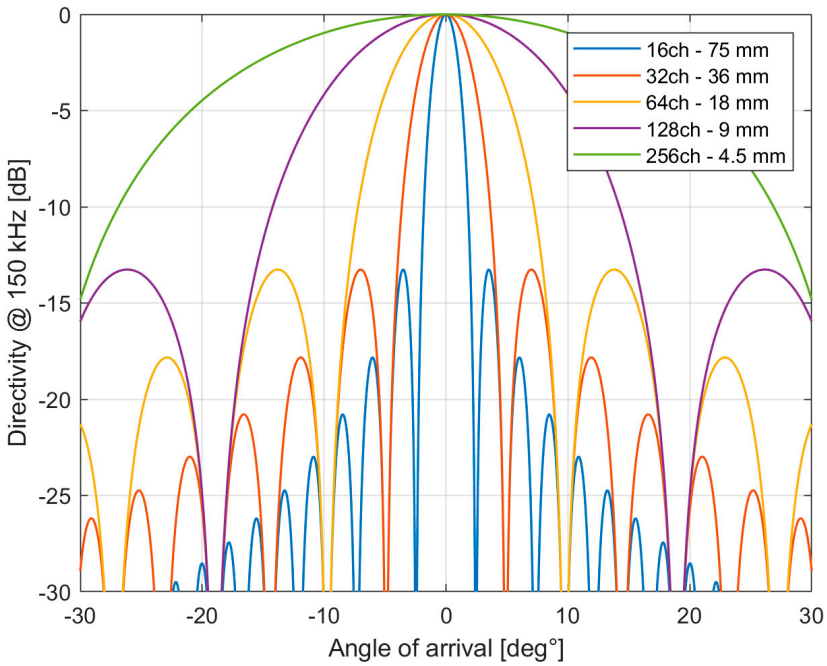

Figure 3. Directivity patterns for different channel widths at 50 kHz (**top**) and 150 kHz (**bottom**), representing center and upper limits of bandwidth for 200 MeV protons.

In this context, a sensor with a constant total area, fixed according to the system noise requirements, is considered, as shown in Figure 4. This total area is divided into a variable number of channels, and how the final acoustic image was affected by the number of channels and the size of the single channel has been studied. Larger sensors will be more directive and will therefore only observe the area in front of them while attenuating signals coming from large angles of arrival. However, if a greater number of smaller channels leads to a more accurate image, it also requires an additional hardware effort to process a greater number of channels in parallel.

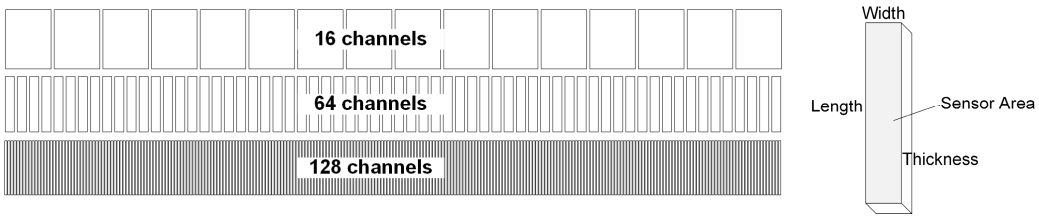

Figure 4. Multichannel array design with same total area divided into different numbers of channels and close −up of single-channel layout.

2.3. Imaging and Gamma Index

To find the optimal sizing of the array, we used the gamma index as an objective tool to measure the quality of the reconstructed image as the number and size of the channels varied. In medical physics, the γ-index is a widely used metric to compare a calculated dose distribution with a reference dose distribution [22]. The γ-index combines both dose difference and distance-to-agreement criteria into a single metric. For each point in the dose distribution, γ is calculated as follows [22]:

$$\gamma(r) = \underset{r' \in v}{min} \sqrt{\left(\frac{D(r) - D'(r')}{\Delta D}\right)^2 + \left(\frac{r - r'}{\Delta d}\right)^2} \tag{8}$$

where D(r) is the dose at position r in the evaluated distribution, D′(r′) is the dose at position r′ in the reference distribution, V is the total volume (or area for 2D distributions)

around r, and ΔD and Δd are, respectively, the dose difference and distance-to-agreement criteria. A γ-index value of $\gamma \leq 1$ indicates that the reconstructed dose at point r is within the acceptable range of the reference dose [23], considering both dose and spatial criteria, set as 3%/3 mm in this work.

3. Results

Figure 5 shows the imaging result for different numbers of sensors, from 16 to 256. As can be seen, for a low number of sensors, the image is very distorted and gradually improves as the number of sensors increases. It can be noted that the quality of each image is not homogeneous. In fact, the central area of the circle has less distortion than the more peripheral regions. This effect is due to the directivity of the sensors, which receive signals perfectly in phase from the center of the circle (0° angle of arrival) and increasingly out of phase at larger angles (outer portions of the circle). This effect is clearly visible for 16 and 32 channels, with the difference in the diameter of the reconstructed beam changing radically between the center of the circumference and the outer regions.

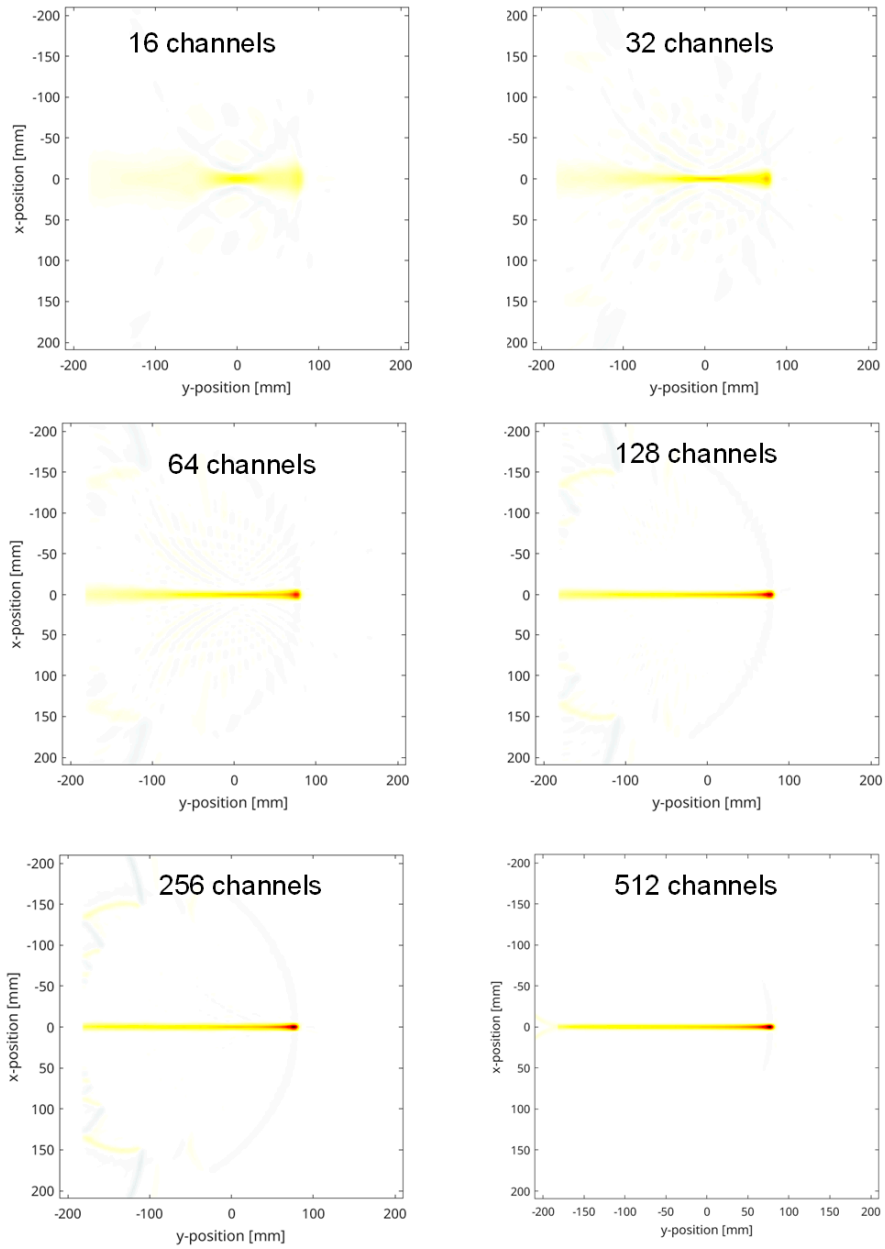

Figure 5. Reconstructed dose deposition for different channel numbers in array.

As the number of channels increases, the region in which the beam is reconstructed with greater accuracy becomes larger and larger, and from 64 channels onwards, the Bragg peak is clearly distinguishable. In each image, the initial part of the range is the one that is most difficult to reconstruct, both because it is the most external and because of the absence of channels in the input window region, which causes a loss of information since a part of the wavefront is not acquired. It can also be noted that due to the destructive interference that occurs with very directive sensors, the amplitude of the images reconstructed with a low number of channels is lower than that with a higher number of channels. Since the total array noise is by design the same in each scenario (as it depends on the total area being held constant), there is a loss of signal-to-noise ratio for low channel numbers, with a consequent further decrease in precision in the reconstructed image due to random noise fluctuations.

Figure 6 shows the gamma index map as the number of sensors varies, computed along the beam range.

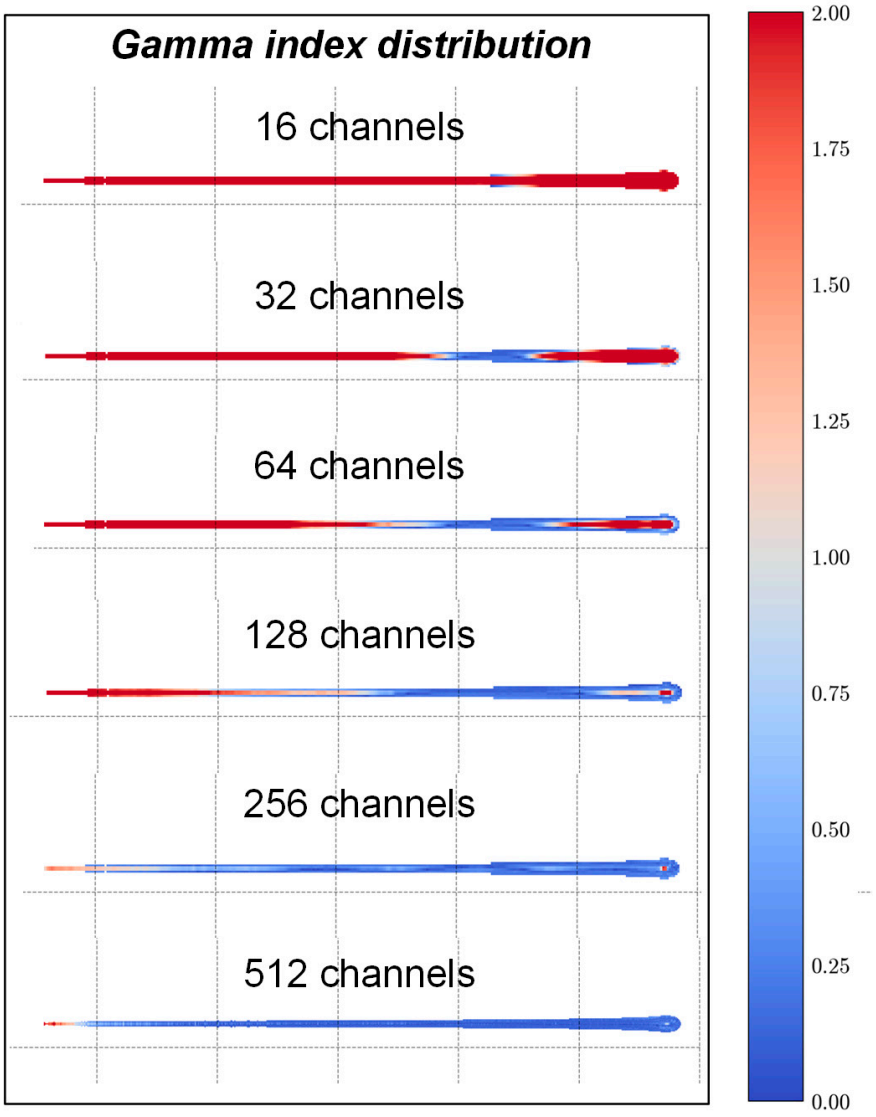

Figure 6. Gamma index map for different channel numbers in array.

As expected from the acoustic images, for 16 and 32 channels, most of the voxels have a gamma index higher than 1. As the number of channels increases, the number of voxels with a gamma index lower than 1 also increases, starting from the central regions of the circumference and gradually covering both the Bragg peak region and the beginning of

the proton range, which is confirmed to be the area most subject to error both due to its proximity to the edge of the circumference and the presence of the beam entrance window.

Figure 7 shows the trend of the percentage of pixels with a gamma index lower than one as the number of channels varies. It can be seen that for a number of channels lower than 100, most of the pixels have a gamma value higher than 1, while when exceeding 200, most of the pixels have an acceptable error. In particular, the commonly accepted threshold of 90% is reached with a number of channels approximately equal to 256, representing a tradeoff between acceptable accuracy and hardware complexity. Finally, Figure 8 shows a detailed view of the reconstructed acoustic image and the gamma index map compared with the original dose deposition.

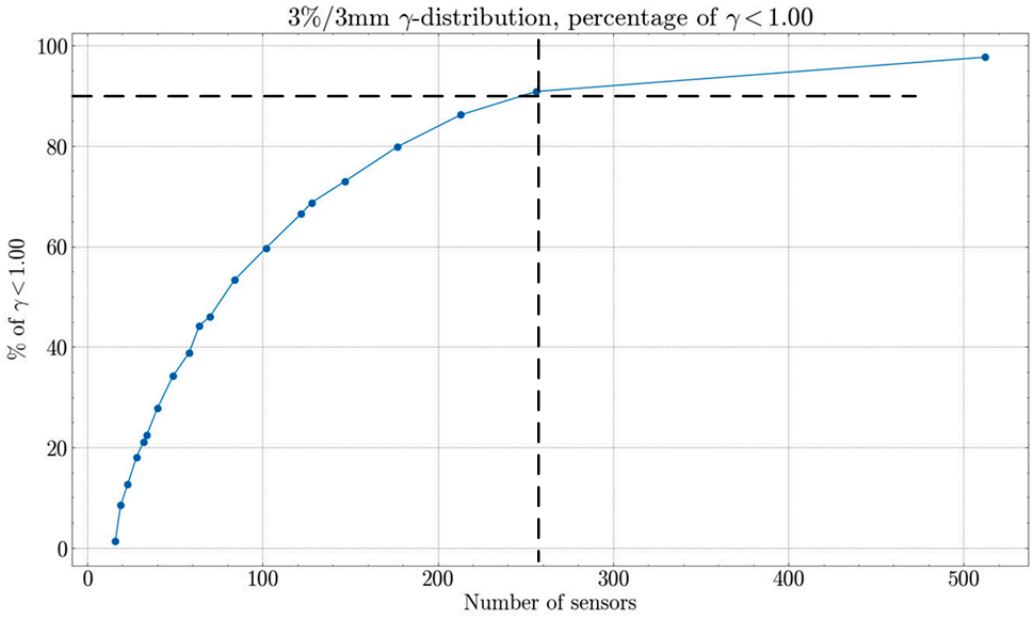

Figure 7. Percentage of pixels with gamma < 1 versus number of sensors in array. Typically used 90% threshold highlighted, met at around 256 channels.

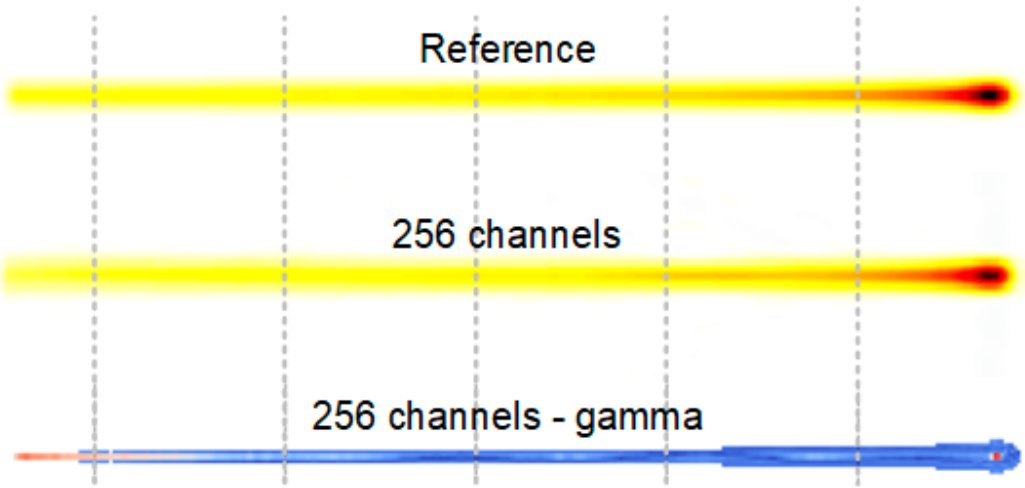

Figure 8. Closeup of reconstructed dose deposition and gamma index map vs. original dose deposition for reference.

4. Conclusions

In this work, it has been highlighted how the array design impacts its ability to reconstruct the dose deposition accurately and sufficiently for the clinical standards represented by the gamma index. What emerges is that in order to operate in clinical contexts, a leap

forward in the technology of ionoacoustic detectors is necessary so they can process in parallel the hundreds of channels necessary to obtain an accuracy sufficient to compete with other nuclear imaging techniques. The natural direction of this technology is to exploit dedicated integrated circuits as the only possible solution to manage such a large number of channels in parallel while maintaining acceptable performance and limited size [23–27].

Author Contributions: Conceptualization, E.A.V.; Methodology, A.M.F.; Writing—original draft, E.A.V.; Writing—review & editing, A.M.F. and M.T.; Supervision, M.D.M. and M.M.; Project administration, E.A.V. All authors have read and agreed to the published version of the manuscript.

Funding: This research was supported by the IONOTRACK project funded by the Italian Institute for Nuclear Physics, Scientific Committee 5 (INFN CSN5).

Data Availability Statement: The raw data supporting the conclusions of this article will be made available by the authors on request.

Conflicts of Interest: The authors declare no conflicts of interest.

References

1. Knoll, G.F. Radiation Sources. In *Radiation Detection and Measurement*; John Wiley & Sons: Hoboken, NJ, USA, 2000; ch. 1, pp. 1–28.
2. Parodi, K.; Polf, J.C. In vivo range verification in particle therapy. *Med. Phys.* **2018**, *45*, e1036–e1050. [CrossRef] [PubMed]
3. Min, C.H.; Kim, C.H.; Youn, M.Y.; Kim, J.W. Prompt gamma measurements for locating the dose falloff region in the proton therapy. *Appl. Phys. Lett.* **2006**, *89*, 1–3. [CrossRef]
4. Hueso-González, F.; Rabe, M.; Ruggieri, T.A.; Bortfeld, T.; Verburg, J.M. A full-scale clinical prototype for proton range verification using prompt gamma-ray spectroscopy. *Phys. Med. Biol.* **2018**, *63*, 185019. [CrossRef] [PubMed]
5. Mirandola, A.; Molinelli, S.; Vilches Freixas, G.; Mairani, A.; Gallio, E.; Panizza, D.; Russo, S.; Ciocca, M.; Donetti, M.; Magro, G.; et al. Dosimetric commissioning and quality assurance of scanned ion beams at the Italian National Center for Oncological Hadrontherapy. *Radiat. Meas. Phys.* **2015**, *42*, 5287–5300. [CrossRef]
6. Sulak, L.; Armstrong, T.; Baranger, H.; Bregman, M.; Levi, M.; Mael, D.; Strait, J.; Bowen, T.; Pifer, A.E.; Polakos, P.A.; et al. Experimental studies of the acoustic signature of proton beams traversing fluid media. *Nucl. Instrum. Methods* **1979**, *161*, 203–217. [CrossRef]
7. Hayakawa, Y.; Tada, J.; Arai, N.; Hosono, K.; Sato, M.; Wagai, T.; Tsuji, H.; Tsujii, H. Acoustic pulse generated in a patient during treatment by pulsed proton radiation beam. *Radiat. Oncol. Investig.* **1995**, *3*, 42–45. [CrossRef]
8. Assmann, W.; Kellnberger, S.; Reinhardt, S.; Lehrack, S.; Edlich, A.; Thirolf, P.G.; Moser, M.; Dollinger, G.; Omar, M.; Ntziachristos, V.; et al. Ionoacoustic characterization of the proton Bragg peak with sub-millimeter accuracy. *Med. Phys.* **2015**, *42*, 567–574. [CrossRef]
9. Lehrack, S.; Assmann, W.; Bender, M.; Severin, D.; Trautmann, C.; Schreiber, J.; Parodi, K. Ionoacoustic detection of swift heavy ions. *Nucl. Instrum. Methods Phys. Res. Sect. A Accel. Spectrometers Detect. Assoc. Equip.* **2020**, *950*, 162935. [CrossRef]
10. Vallicelli, E.A.; Baschirotto, A.; Lehrack, S.; Assmann, W.; Parodi, K.; Viola, S.; Riccobene, G.; De Matteis, M. 22 dB signal-to-noise ratio real-time proton sound detector for experimental beam range verification. *IEEE Trans. Circuits Syst. I Regul. Pap.* **2020**, *68*, 3–13. [CrossRef]
11. Wang, S.; Gonzalez, G.; Sun, L.; Xu, Y.; Pandey, P.; Chen, Y.; Xiang, S. Real-time tracking of the Bragg peak during proton therapy via 3D protoacoustic Imaging in a clinical scenario. *NPJ Imaging* **2024**, *2*, 34. [CrossRef]
12. Samant, P.; Trevisi, L.M.; Chen, Y.; Zwart, T.; Xiang, L. 3-D Protoacoustic imaging through a planar ultrasound array: A simulation Workflow. *IEEE Trans. Radiat. Plasma Med. Sci.* **2022**, *7*, 83–95. [CrossRef] [PubMed]
13. Yu, Y.; Li, Z.; Zhang, D.; Xing, L.; Peng, H. Simulation studies of time reversal-based protoacoustic reconstruction for range and dose verification in proton therapy. *Med. Phys.* **2019**, *46*, 3649–3662. [CrossRef] [PubMed]
14. Schauer, J.; Wieser, H.P.; Huang, Y.; Ruser, H.; Lascaud, J.; Würl, M.; Chmyrov, A.; Vidal, M.; Herault, J.; Ntziachristos, V.; et al. Proton beam range verification by means of ionoacoustic measurements at clinically relevant doses using a correlation-based evaluation. *Front. Oncol.* **2022**, *12*, 925542. [CrossRef] [PubMed]
15. Lascaud, J.; Dash, P.; Wieser, H.P.; Kalunga, R.; Würl, M.; Assmann, W.; Parodi, K. Investigating the accuracy of co-registered ionoacoustic and ultrasound images in pulsed proton beams. *Phys. Med. Biol.* **2021**, *66*, 185007. [CrossRef] [PubMed]
16. Patch, S.K.; Hoff, D.E.; Webb, T.B.; Sobotka, L.G.; Zhao, T. Two-stage ionoacoustic range verification leveraging Monte Carlo and acoustic simulations to stably account for tissue inhomogeneity and accelerator–specific time structure—A simulation study. *Med. Phys.* **2018**, *45*, 783–793. [CrossRef]
17. Takayanagi, T.; Uesaka, T.; Nakamura, Y.; Unlu, M.B.; Kuriyama, Y.; Uesugi, T.; Ishi, Y.; Kudo, N.; Kobayashi, M.; Umegaki, K.; et al. On-line range verification for proton beam therapy using spherical ionoacoustic waves with resonant frequency. *Sci. Rep.* **2020**, *10*, 20385. [CrossRef]
18. Lascaud, J.; Dash, P.; Würl, M.; Wieser, H.P.; Wollant, B.; Kalunga, R.; Assmann, W.; Clevert, D.A.; Ferrari, A.; Sala, P.; et al. Enhancement of the ionoacoustic effect through ultrasound and photoacoustic contrast agents. *Sci. Rep.* **2021**, *11*, 2725. [CrossRef]

19. Lehrack, S.; Assmann, W.; Bertrand, D.; Henrotin, S.; Herault, J.; Heymans, V.; Vander Stappen, F.; Thirolf, P.G.; Vidal, M.; Van de Walle, J.; et al. Submillimeter ionoacoustic range determination for protons in water at a clinical synchrocyclotron. *Phys. Med. Biol.* **2017**, *62*, L20. [CrossRef]
20. Ketterling, J.A.; Aristizabal, O.; Turnbull, D.H.; Lizzi, F.L. Design and fabrication of a 40-MHz annular array transducer. *IEEE Trans. Ultrason. Ferroelectr. Freq. Control* **2005**, *52*, 672–681. [CrossRef]
21. Ambrosy, A.; Holdik, K. Piezoelectric PVDF films as ultrasonic transducers. *J. Phys. E Sci. Instrum.* **1984**, *17*, 856. [CrossRef]
22. Hussein, M.; Clark, C.; Nisbet, A. Challenges in calculation of the gamma index in radiotherapy—Towards good practice. *Phys. Medica* **2017**, *36*, 1–11. [CrossRef] [PubMed]
23. Vallicelli, E.A.; De Matteis, M. Analog filters design for improving precision in proton sound detectors. *J. Low Power Electron. Appl.* **2021**, *11*, 12. [CrossRef]
24. De Matteis, M.; Baschirotto, A.; Vallicelli, E.; Zanini, E. Proton-Induced Thermoacoustic Process as Linear-Time-Invariant System. *IEEE Trans. Radiat. Plasma Med. Sci.* **2021**, *6*, 336–344. [CrossRef]
25. Riva, M.; Vallicelli, E.A.; Baschirotto, A.; De Matteis, M. Acoustic analog front end for proton range detection in hadron therapy. *IEEE Trans. Biomed. Circuits Syst.* **2018**, *12*, 954–962. [CrossRef]
26. De Matteis, M.; Galante, N.; Fary, F.; Vallicelli, E.; Baschirotto, A. 64 dB dynamic-range 810 µW 90 MHz fully-differential flipped-source-follower analog filter in 28 nm-CMOS. *IEEE Trans. Circuits Syst. II Express Briefs* **2021**, *68*, 3068–3072.
27. Vallicelli, E.A.; Turossi, D.; Gelmi, L.; Baù, A.; Bertoni, R.; Fulgione, W.; Quintino, A.; Corcione, M.; Baschirotto, A.; De Matteis, M. A 0.3 nV/$\sqrt{}$ Hz input-referred-noise analog front-end for radiation-induced thermo-acoustic pulses. *Integration* **2020**, *74*, 11–18. [CrossRef]